Journal Name

ARTICLE

Magnetic anisotropy of two tetrahedral Co(II)-halide complexes with triphenylphosphine ligands

Received 00th January 20xx,
Accepted 00th January 20xx

DOI: 10.1039/x0xx00000x

www.rsc.org/

Wei Lv,[a] Hui-Hui Cui,[a] Lei Chen,[b] Yi-Quan Zhang,*[c] Xue-Tai Chen,*[a] Zhenxing Wang,*[d] Zhong-Wen Ouyang[d] and Zi-Ling Xue[e]

Recently, the choice of ligand and geometric control of mononuclear complexes, which can affect the relaxation pathways and blocking temperature, have received wide attention in the field of single ion-magnets (SIMs). To find out the influence of the cooordination environment on SIMs, two four-coordinate mononuclear Co(II) complexes $[NEt_4][Co(PPh_3)X_3]$ (X = Cl^-, **1**; Br^-, **2**) have been synthesized and studied by X-ray single crystallography, magnetic measurement, high-frequency and -field EPR (HF-EPR) spectroscopy and theoretical calculations. Both complexes are in a cubic space group $Pa\bar{3}$ (No. 205), containing a slightly distorted tetrahedral moiety with crystallographically-imposed C_{3v} symmetry through the $[Co(PPh_3)X_3]^-$ anion. The direct-current (dc) magnetic data and HF-EPR spectroscopy indicated the anisotropic S = 3/2 spin ground states of the Co(II) ions with the easy-plane anisotropy for **1** and **2**. Ab initio calculations were performed to confirm the positive magnetic anisotropies of **1** and **2**. Frequency- and temperature-dependent alternating-current (ac) magnetic susceptibility measurements revealed slow magnetic relaxation for **1** and **2** at an applied dc field. Finally, the magnetic properties of **1** and **2** were compared to other Co(II) complexes with $[CoAB_3]$ moiety.

Introduction

Single-molecule magnets (SMMs)[1, 2] have been a hot topic in the area of molecular magnetism due to their potential applications in molecular spintronics, ultra-dense information storage and quantum computing.[3-5] Extensive studies have been performed on the SMMs based on polynuclear transition metal clusters with a large spin (S) ground state. The effective energy barrier U_{eff} is determined by the axial zero-field splitting (ZFS) parameter D and the spin of the ground state (S) via $U_{eff} = |D|S^2$ for the molecules with integer spin ground state and $U_{eff} = |D|(S^2 - 1/4)$ for those with half-integer spin ground state. Importantly, it has been proved difficult to enlarge the energy barrier by only increasing the spin of the ground state in polynuclear complexes of transition metals since the D value typically decreases with increasing the value of S.[6]

Thus, recent efforts have been devoted to those SMMs containing one paramagnetic lanthanide[7, 8] or transition-metal ion,[9-11] which are termed single-ion magnets (SIMs). The priority in the current SIM studies is to create the conditions for the unique metal ion to manifest the high magnetic anisotropy. The SIMs are the simplest systems in which magnetic anisotropy and magnetic dynamics can be fine-tuned via the variation of the ligand field around the metal centre.

To date, a large number of SIMs based on the first-row transition metal complexes have been reported.[9-11] The anisotropic Co(II) complexes have been heavily studied with the results of various Co(II)-based SIMs with different coordination geometries and environments,[12-19] among which the four-coordinate Co-SIMs are of particular interest. Most of the reported four-coordinate Co(II)-SIMs usually contain a mixed donor set from N, P, As, O, S, Se and/or halides with the coordination moieties such as $[CoN_2N'_2]$,[20,21] $[CoNN'_3]$,[17,22,23] $[CoN_2O_2]$,[24-26] $[CoN_2S_2]$,[27] $[CoL_2X_2]$ (L_2 = N_2,[28, 29] P_2,[30-37] O_2,[38] S_2,[39, 33] C_2,[41] X = halide), $[CoN_3X]$,[42] and $[CoNX_3]$.[43] The other family includes a smaller number of homoleptic SIMs containing a CoX_4 unit (X = O,[44] S,[45] Se,[46] Te,[47] N,[48] Cl[48]) with four identical donors.

It is known that the coordination environment plays a key role in determining the magnetic anisotropy. However, it has been proved difficult to predict the magnetic anisotropy. But people never stop trying to find out the factors involved such as the coordination number, ligand and electronic structures of paramagnetic centers.[17] During the period of our research on four-coordination Co(II)–SIMs, we noticed that Co(II)-SIMs with the $[CoAB_3]$ moiety usually have nitrogen-containing ligands such as $[CoNN'_3]$,[17,22,23] $[CoN_3X]$,[42] and $[CoNX_3]$.[43] Furthermore, they exhibit

[a] State Key Laboratory of Coordination Chemistry, School of Chemistry and Chemical Engineering, Nanjing University, Nanjing 210023, China. E-mail: xtchen@nju.edu.cn.
[b] School of Environmental and Chemical Engineering, Jiangsu University of Science and Technology, Zhenjiang 212003, China.
[c] Jiangsu Key Laboratory for NSLSCS, School of Physical Science and Technology, Nanjing Normal University, Nanjing 210023, China
[d] Wuhan National High Magnetic Field Center& School of Physics, Huazhong University of Science and Technology, Wuhan 430074, China
[e] Department of Chemistry, University of Tennessee, Knoxville, Tennessee 37996, USA.

†Electronic supplementary information (ESI) available: Table for the summary of crystal data and refinement for **1** and **2**; Table for the calculations by SHAPE; Table for the fitting data for the Cole-Cole plot; Table for the theoretical calculation data; Figures of XRD patterns for **1-2**; Additional figures for magnetic characterization, HFEPR data and theoretical calculations; Additional structural data in CIF format (CIF). See DOI: 10.1039/x0xx00000x

two coordination geometries, distorted tetrahedron for $[CoN_3X]$,[41] and $[CoNX_3]$[43] and trigonal monopyramid for $[CoNN'_3]$[17,22,23] (Table S1, ESI). The four-coordinate Co(II)-SIMs with phosphorus ligands have been relatively less studied. Only those with the $[CoP_2X_2]$ core are known,[30-37] which are summarized in Table S2, ESI). Thus, we have synthesized two Co(II) complexes with the $[CoPX_3]^-$ (X = halide) moiety, in which the Co(II) centre is coordinated with one triphenylphosphine and three halogen ligands. To our knowledge, such complexes have not been studied as SIM candidates. Here, we present the synthesis and structures of tetrahedral Co(II) complexes $[NEt_4][Co(PPh_3)X_3]$ (X = Cl^-, **1** and Br^-, **2**). By analysing the direct-current (dc) magnetic data, **1** and **2** exhibit easy-plane magnetic anisotropy with the *D* values of +21.15(7) and +14.34(5) cm^{-1}, respectively. The easy-plane anisotropic nature has been confirmed by high-field and high-frequency electron paramagnetic resonance (HF-EPR) spectroscopy and theoretical calculations. Alternating-current (ac) magnetic susceptibility measurements demonstrated the field-induced slow magnetization relaxation in **1** and **2**.

Experimental

Synthesis and general characterization

All solvents and other chemicals were commercially available and used without further purification. Elemental analyses were performed on an Elementar Vario ELIII elemental analyser. Powder X-ray diffraction (PXRD) patterns were recorded on a Bruker D8 ADVANCE X-ray powder diffractometer with a Cu Kα X-ray source (λ = 1.54056 Å) operated at 40 kV and 40 mA.

Synthesis of complexes 1 and 2

Complexes **1** and **2** were prepared according to the modified procedure.[48]

$(Et_4N)[Co(PPh_3)Cl_3]$ (1). Tetraethylammonium chloride (5.0 mmol, 0.83 g) and triphenylphosphine (5.0 mmol, 1.31 g) were dissolved in 20 mL of newly purchased or freshly distilled n-butanol. The mixture was stirred and heated until the solution was clear. The solution of $CoCl_2{\cdot}6H_2O$ (5.0 mmol, 1.19 g) in 25 mL of n-butanol was added to the above solution and boiled for 30 minutes. Then, the reaction mixture was cooled slowly to room temperature to give a cyan precipitate. The precipitate was extracted into 20 mL of CH_3CN and filtered to yield a cyan solution. The blue crystals suitable for X-ray single-crystal structure determination were obtained by the slow diffusion of the vapour of diethyl ether into the acetonitrile solution with a yield of 67% based on Co. Anal. calc. for $C_{26}H_{35}Cl_3CoNP$: C, 55.98; H, 6.32; N, 2.51. Found: C, 56.35; H, 6.37; N, 2.55.

$(Et_4N)[Co(PPh_3)Br_3]$ (2). $Co(NO_3)_2{\cdot}6H_2O$ (5 mmol, 1.46 g) and KBr (10 mmol, 1.19 g) were dissolved in 25 mL of newly purchased or freshly distilled n-butanol. The solution was boiled and stirred under 120 °C for 3 h. Then the resulting white solid was removed to give a purple filtrate after the mixture was cooled to room temperature. The filtrate was added to the solution of tetraethylammonium bromide (5.0 mmol, 1.04 g) and triphenylphosphine (5.0 mmol, 1.31 g) in 20 mL of n-butanol. The mixture was stirred overnight to give a microcrystalline solid. The precipitate was filtrated and dissolved in 40 mL of CH_3CN. The cyan block crystals were obtained by evaporation under N_2 for one week, in a yield of 71% based on Co. Anal. Calc. for $C_{26}H_{35}Br_3CoNP$: C, 45.18; H, 5.10; N, 2.03. Found: C, 45.54; H, 5.21; N, 2.06.

X-ray single-crystal structure determination

Single-crystal X-ray crystallographic data for **1** and **2** were collected by using a Bruker APEX DUO diffractometer at 296 K with a CCD area detector (Mo Kα radiation, λ = 0.71073 Å).[50] The APEXII program was used for collecting frames of data and determining the unit cell parameters. The data were integrated with SAINT program[51] and corrected for Lorentz factor and polarization effects. The absorption corrections were applied using SADABS.[52] The molecular structures were solved and completed via full-matrix least-squares procedure SHELXL (*version 2018/3*).[53] The Co atom was determined first using the difference Fourier maps and then the other non-hydrogen atoms were subsequently identified. All non-hydrogen atoms were refined anisotropically and hydrogen atoms were set and generated as riding on the corresponding non-hydrogen atoms.

Magnetic measurements

Magnetic measurements were performed using a vibrating sample magnetometer (VSM) of Quantum Design MPMS SQUID-VSM system. Variable-temperature dc susceptibility data of **1** and **2** were collected under a field of 0.10 T in the range of 2.0-300 K. The field-dependent magnetizations were measured in the range of 1-7 T at 1.8 K, 3.0 K and 5.0 K. Alternating-current (ac) susceptibility measurements were carried out on vibrating sample magnetometer (VSM) of Quantum Design PPMS system with an oscillating ac field of 1200 Oe for **1** and 1500 Oe for **2**, respectively, at frequencies ranging from 10 to 10000 Hz. All magnetic susceptibilities data were corrected for the diamagnetic contributions of the sample holder as well as for diamagnetism of the sample using Pascal's constants.[54]

HF-EPR measurements

HF-EPR spectra were recorded on a locally developed spectrometer with a pulse magnetic field at the Wuhan National High Magnetic Field Center, China.[55,56] The microwaves of the transmission-type instrument are propagated by over-sized cylindrical light pipes. The samples were measured with KBr and pressed into pellets to minimize the effect of field-induced torquing.

Results and discussion

Description of the crystal structures

The crystal structure of **1**, which was prepared by a different method, was determined at room temperature by Li et al.[57] We re-determined the structure of **1** along with **2** for comparison. As illustrated in Table S3 (ESI), both complexes **1** and **2** crystallize in the cubic space group $Pa\bar{3}$ (No. 205) with eight molecules in the unit cell. SMMs with cubic symmetry are rare. Both complexes adopt a distorted tetrahedral coordination geometry surrounding the Co center, each of which is ligated by a PPh_3 ligand and three halogen anions X (X = Cl^- for **1** and Br^- for **2**). The overall one negative charge is neutralized by a Et_4N^+ cation.

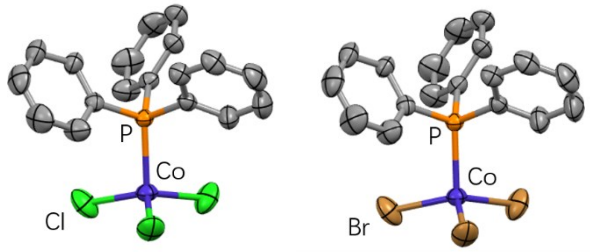

(a) (b)

Fig. 1 Structures of the anions in **1** and **2.** Red, yellow, green, orange and gray spheres represent Co, P, Cl, Br and C atoms. H atoms are omitted for clarity.

The selected bond lengths and bond angels are listed in Table S4 (ESI). The Co-P bond lengths are similar in **1** (2.3763(16) Å) and **2** (2.373(3) Å). The Co-Cl bond length of **1** (2.2508(12) Å) is shorter than the Co-Br bond length of **2** (2.3827(10) Å) due to the different radii of these two halide anions. The X-Co-X angles (114.11(4)°) and the P-Co-X angles (104.30(5)°) in **1** are also similar to the corresponding values in complex **2** (113.39(4)° and 105.19(5)°, respectively). These bond angles deviate significantly from the ideal angle of 109.5° for a perfect tetrahedron. These bond parameters of **1** and **2** are comparable to those reported for the Co(II) complexes with $[CoPX_3]$ (X = Cl, Br) moiety.[58-64]

There is a C_3 axis going through the Co-P bond in the anions of molecules of **1** and **2**, in which the $[CoPX_3]^-$ moiety possesses crystallographically imposed C_{3v} symmetry. The continuous shape measure (*CShM*) analyses with Shape 2.1[65,66] have been performed to evaluate the degree of deviation with respect to an ideal tetrahedron. The deviation values are 0.177 and 0.199 for **1** and **2** (Table S4), respectively, as a result of the deviation from the ideal tetrahedron.

The closest intermolecular Co···Co distances are 9.02(3) Å for **1** and 9.18(2) Å for **2**. No other interaction including hydrogen bond was observed, except for van der Waals interactions in the crystal lattice of both complexes.

Static magnetic properties

The static magnetic properties of **1** and **2** were studied by dc magnetic measurements on polycrystalline powders of **1** and **2** at an applied dc field of 0.1 T between 2.0 K and 300 K (Fig. 2). The room temperature magnetic susceptibility-temperature products, $\chi_M T$, are 2.50 and 2.46 cm^3 K mol^{-1} for **1** and **2**, respectively, corresponding to the value for an $S = 3/2$ ion with $g = 2.31$ and 2.29. These observed $\chi_M T$ products are much higher than the spin-only value of 1.875 cm^3 mol^{-1} K expected for an $S = 3/2$ system ($g = 2.0$), indicating a sizable contribution of orbital angular momentum. **1** and **2** exhibit similar trends in the $\chi_M T$-T plots. Upon cooling, the $\chi_M T$ products for both **1** and **2** decrease gradually to about 75 K, after which they decrease rapidly to the minimum values of 1.43 cm^3 K mol^{-1} and 1.46 cm^3 mol^{-1} K at 2 K, respectively. The sudden drop in the $\chi_M T$ value below 75 K suggests the presence of a strong magnetic anisotropy rather than the intermolecular interaction considering the long distance between the Co(II) ions.

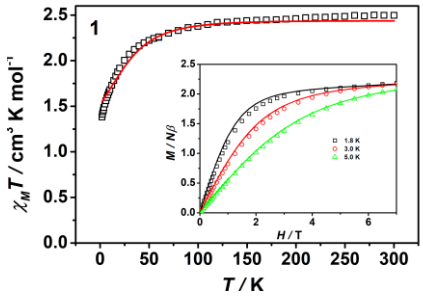

(a)

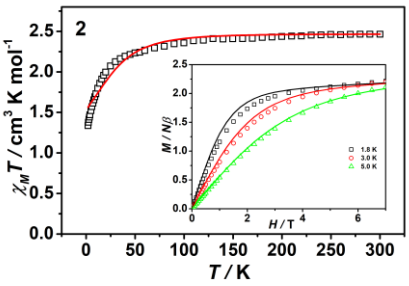

(b)

Fig. 2 Variable-temperature dc susceptibility data of 1 (a) and 2 (b) under 0.10 T applied dc field. Inset: field dependence of the magnetization below 5 K for 1. Solid lines are the fits to the data with program *PHI*.[67]

The field-dependent magnetizations were collected at applied magnetic fields in a range of 1-7 T below 5 K (inset, Fig. 2). The magnetization values are 2.18 $N\mu_B$ and 2.50 $N\mu_B$ for **1** and **2** at 7 T, without reaching saturation. The lack of saturation agrees with the presence of significant magnetic anisotropy.

The static magnetic data of four-coordinate Co(II) complexes are usually modeled by the effective spin-Hamiltonian based on the assumption that the zero-field splitting (ZFS) parameters, axial D and rhombic E, can be used to present their magnetic anisotropy. Our theoretical calculations have showed that the anisotropies of **1-2** can indeed be depicted by zero-field splitting parameters D and E (vide infra). Therefore, both $\chi_M T$ versus T and M versus H curves were fit simultaneously with the following spin Hamiltonian (eqn. 1) employing the *PHI* program[66],

$$H = D\left(\hat{S_z}^2 - S(S+1)/3\right) + E\left(\hat{S_x}^2 - \hat{S_y}^2\right) + \mu_B g \hat{S} B \quad (1)$$

where μ_B is the Bohr magneton, g is a tensor, B is the magnetic field vector. Because of the crystallographically imposed C_{3v} symmetry of these two anions, the rhombic term in eqn. 1 is zero when Jahn-Teller distortion is ignored. Thus E was fixed as zero and $g_x = g_y$ in the fitting. Three parameters were employed in the fitting of magnetic data, resulting in a positive D value but $g_z > g_x(g_y)$. Such unreasonable parameters might be due to the high number of the fitting parameters. Therefore, due to the agreement between the calculated magnetic susceptibilities curve by NEVPT2 method and the experimental curve (vide infra, Fig. S13, ESI), the calculated g values were employed as the value for the fitting. Thus, we fix g_x =

g_y = 2.236, g_z = 2.103, and only D was varied to simultaneously fit the data,[67] giving D = +42.8(7) cm^{-1}. Similar analysis of the magnetic data of **2** gave D = +41.2(9) cm^{-1}. The positive sign of D values was further confirmed by the fact that the fitting could not give the reasonable agreement when the D value was set as negative. These results indicate the significant easy-plane anisotropy for **1** and **2**. In order to check the accuracy of the set of fitted values, the survey feature of the PHI code[66] was employed. The resulting survey plots are shown in Figs, S3-S4, in which the fitting values are clearly located in a narrow region of residue minimums.

HFEPR spectroscopy

High-field and -frequency electron paramagnetic resonance (HFEPR) spectra were recorded on the polycrystalline samples of **1** and **2** at different frequencies in order to confirm the positive nature of D parameters.

There are two features observed in the spectra of **1** at the frequency from 60 to 420 GHz at 2 K. A typical spectrum at 60 GHz is shown in Fig. 3a, in agreement with the axial symmetry of **1** and **2**. A 2D resonating field versus frequency curve was established based on these spectra, in which the observed experimental points are located in two straight lines. These experimental observations indicated that only intra-Kramers transitions within the lowest doublet M_S = ±1/2 with ΔM_S = ±1 were observed due to the large zero-field splitting. The absence of inter-Kramers transition(s) in the high-frequency and -field conditions between the ±3/2 and ±1/2 doublets puts a lower limit on 2|D| > 14 cm^{-1}. Because of the positive and large D value, only the Kramers doublet is populated at 2 K. These HFEPR spectra can be interpreted as an effective spin doublet (S_{eff} = 1/2) with strongly anisotropic g_{eff} factor. The effective g values [g_{xeff} = g_{yeff} = 4.40, g_{zeff} = 2.04] are in accord with a positive sign of D parameter for a spin 3/2 system.

A 2D resonating field versus frequency curve was fit by the spin-Hamiltonian as shown in eqn (1) via the *Spin* program.[68] Given the magnitude of D from the fitting of the dc magnetic data (D = 42.8 cm^{-1}, E = 0 cm^{-1}), the simulations were conducted assuming an axial g-tensor (g_x = g_y), yielding the parameters g_x = g_y = 2.30, g_z = 2.08. In addition, by comparing the experimental spectrum to the simulated ones obtained with both positive and negative D values (Fig. 3a), the sign of D value was confirmed to be positive rather than negative.

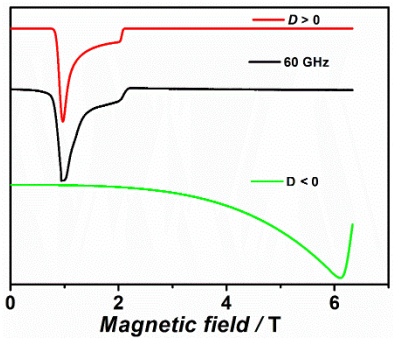

(a)

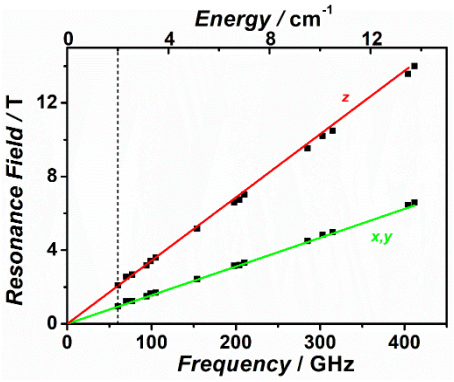

(b)

Fig. 3 (a) Typical HFEPR spectrum of **1** at 2 K (black) with the simulations using spin Hamiltonian with the true spin S = 3/2 (red: D > 0; green: D < 0). (b) Resonance field vs. microwave frequency for EPR transitions for **1** at 2 K. The squares are the experimental points while green, blue, and red curves are generated by fitting using program *SPIN*[68] with the magnetic field parallel to the *x*, *y*, and *z* axes of the ZFS tensor, respectively.

Similarly, two broad features were observed in the HFEPR spectra of **2** at the frequency from 60 to 420 GHz at 2 K. The spectrum at 154 GHz is shown in Fig. 4(a) and the 2D resonating field versus frequency curve is shown in Fig 4(b). Again, these two features can be modeled as an effective spin doublet (S_{eff} = 1/2) with a strongly anisotropic g_{eff} factor [g_{xeff} = g_{yeff} = 4.10, g_{zeff} = 1.88], in agreement with the positive sign of D parameter for a high-spin Co(II) ion. The 2D resonating field versus frequency curve was fit by the spin-Hamiltonian in eqn (1) by the *Spin* program[63] to give the parameters D = 41.2 cm^{-1} (fixed), E = 0 cm^{-1}, g_x = g_y = 2.15, g_z = 2.01. Furthermore, the positive sign was confirmed by the comparison of the experimental spectrum and the simulated ones with positive and negative sign of the D values.

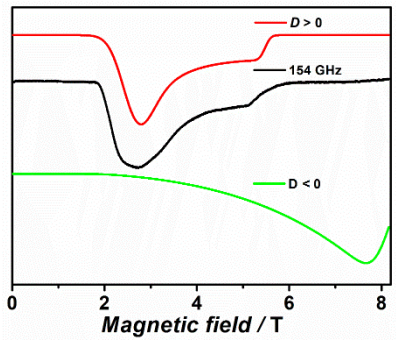

(a)

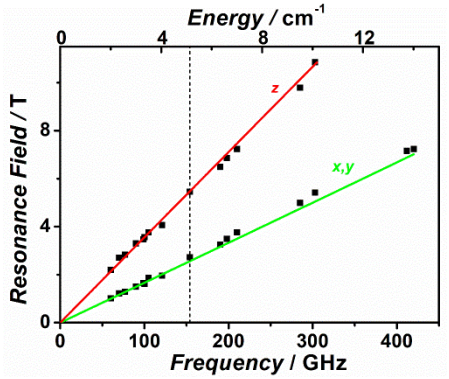

(b)

Fig. 4 (a) Typical HFEPR spectrum of **2** at 2 K (black) with the simulations using spin Hamiltonian with the true spin $S = 3/2$ (red: $D > 0$; green: $D < 0$). b) Resonance field vs. microwave frequency for EPR transitions for **2** at 2 K. The squares are the experimental points while green, blue, and red curves are generated by fitting using the program *SPIN*[67] with the magnetic field parallel to the *x, y*, and *z* axes of the ZFS tensor, respectively.

Dynamic magnetic properties

To investigate the magnetic relaxation dynamics, temperature- and frequency-dependent alternating-current susceptibilities were studied on polycrystalline samples of **1** and **2**. The field-dependent measurements were performed under various dc fields up to 0.25 T at 1.8 K (Fig. S5, ESI†). There was no out-of-phase susceptibility signal under zero static magnetic field. However, significant frequency-dependent out-of-phase signals (χ''_M) were observed for **1** and **2** when a magnetic field was applied, suggesting that **1** and **2** are field-induced SIMs. The data indicate the optimum fields to reduce the QTM effect and finally, we choose 0.12 T and 0.15 T for **1** and **2**, respectively. Therefore, these optimum fields were used for the further temperature- and frequency-dependent ac measurements in the temperature range of 1.8–4.4 K for **1** and 1.8–2.8 K for **2** (Figs. 5, S6 and S7). The peaks of χ_M'' signals for **1** and **2** appear at 891 Hz and 5008 Hz at 1.8 K, respectively. With the increasing of temperature, the peak value of χ''_M shift gradually to the higher frequency region.

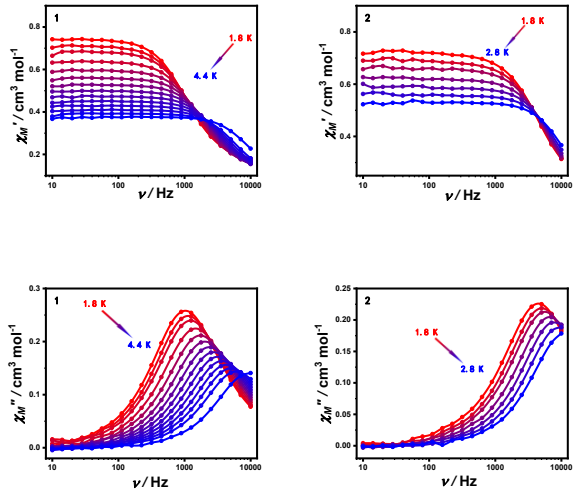

Fig. 5 Frequency dependence of the ac susceptibility from 1.8 K to 4.4 K for **1** at 0.12 T and from 1.8 K to 2.8 K for **2** at 0.15 T. The solid lines are for eye guide.

The Cole–Cole plots (Fig. 6 and S8, ESI†) generated from the ac susceptibility data were fit using the generalized Debye model[69,70] (eqn. 2) to extract the values and distribution of the relaxation times.

$$\chi_{ac}(\omega) = \chi_S + \frac{\chi_T - \chi_S}{1 + (i\omega\tau\ )^{(1-\alpha)}} \qquad (2)$$

where χ_T and χ_S are the isothermal and the adiabatic susceptibility, respectively; ω is angular frequency; τ is the relaxation time; α indicates the deviation from a pure Debye model. The obtained α values for **1** and **2** are in the range of 0.01–0.07 and 7.46×10^{-9}–0.08 (Table S5, ESI†), respectively, indicating the relatively narrow distribution of the relaxation times for **1** and **2**.

Three possible magnetic relaxation mechanisms, *i. e*. thermal-assisted Orbach, Raman and direct processes can occur in **1** and **2**. Our fittings employing the Orbach and/or direct process could not give reasonable results. The plots of $ln(\tau)$ versus T^{-1} were modeled by the power law $\tau^{-1} = CT^n$, yielding $C = 2202.69(1)$ s^{-1} $K^{-1.88}$, $n = 1.88(6)$ for **1** (Fig. 7) and $C = 9035.29(4)$ s^{-1} $K^{-1.96}$, $n = 1.96(9)$ for **2** (Fig. S9, ESI†). The simulated data are in good agreement with the experimental ones but the values of n (1.88 for **1** and 1.96 for **2**) is much less than 9 expected for the Raman process of a Kramers ion. However, the obtained values n for both **1** and **2** are close to 2, indicating that the same types of phonons are involved in the spin-lattice relaxation in these two compounds. This relaxation with n close to 2 cannot be explained by the Raman process,[71,72] but by the phonon bottleneck effect.[73] Similar relaxations have also been suggested for Co(II),[74-78] Mn(II),[76, 81, 82] and Ni(I)[83] systems.

It is important to note that the extracted values from the above fits should be carefully considered since there are only few data points in a narrow temperature range (1.8-4.0 K for **1** and 1.8-2.6 K for **2**).

.

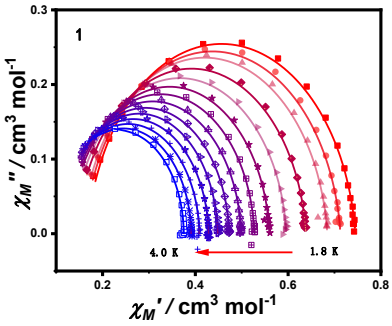

Fig. 6 Cole–Cole plots for **1** under 0.12 T dc field. The solid lines are the best fits to the experiments with the generalized Debye model.

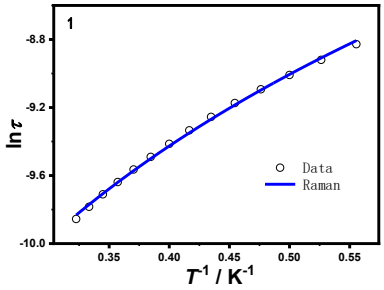

Fig. 7 The plot of ln(*τ*) versus T^{-1} for **1**. The solid blue line represents the best fit by the Raman process.

Theoretical calculations

In order to get an insight into the magnetic ansitropies of **1**-**2**, theoretical studies were performed on **1**-**2** by CASPT2 with MOLCAS 8.4[80] and NEVPT2 with ORCA 4.2.[85] Calculation details are given in ESI.

The energies of the low-lying spin-free states and spin-orbit states were calculated for **1**-**2**. The energy differences between the lowest two spin-free states of **1** and **2** (2817.1 cm^{-1} for **1** and 2684.3 cm^{-1} for **2**, Table S6) are much larger than those between the lowest two spin-orbit states (78.2 cm^{-1} for **1** and 63.6 cm^{-1} for **2**, Table S7). Furthermore, the compositions of the lowest two spin-orbit states arise entirely from the ground spin-free states. Thus, we can use the effective spin-Hamiltanian (eqn 1) with ZFS parameters *D* and *E* to depict their magnetic anisotropies. The calculated *D*, *E* (cm^{-1}) and ***g*** (g_x, g_y, g_z) tensors using CASPT2 and NEVPT2 with MOLCAS 8.4 and ORCA 4.2, respectively, are listed in Table 1. The calculated *D* values obtained using both approaches are positive for **1**-**2**, showing the easy-plane anisotropy. The *D* values obtained by NEVPT2 are smaller than those by CASPT2. These calculated *D* values are close to those determined using the magnetic data.

To deeply analyze magnetic anisotropy, we have calculated the contributions of the excited states (with relative energy, cm^{-1}) to *D* and *E* values for **1** and **2** using NEVPT2 with ORCA 4.2, which are listed in Table S8. The dominant contributions to the positive *D* values are found to arise from the two close quartet states, particularly the second and the third quartet states for both **1** and **2**. The contributions of the second and third quartet states to *E* values cancel out due to the C_3 symmetry for **1** and **2**, resulting in the *E* values being zero.

Table 1. Calculated ZFS parameters *D*, *E* (cm^{-1}) and ***g*** (g_x, g_y, g_z) tensors of the lowest two spin-orbit states of **1** and **2** using CASPT2 and NEVPT2 with MOLCAS 8.4 and ORCA 4.2, respectively.

Complexes	CASPT2				
	D_{cal}	E_{cal}	g_x	g_y	g_z
1	39.1	0.0	2.471	2.460	2.075
2	31.8	0.0	2.462	2.456	2.127
Complexes	NEVPT2				
	D_{cal}	E_{cal}	g_x	g_y	g_z
1	26.8	0.0	2.356	2.355	2.103
2	23.0	0.0	2.362	2.361	2.136

The sign and value of *D* can be rationalized by using a spin-orbit coupling operator.[69] When the spin-conserved excitation occurs between orbitals with the same $|m_l|$ values, the *Ms* = ±3/2 components become more stable, and thus a negative contribution to the *D* value is expected. On the other hand, an excitation between orbitals involving a $\Delta|m_l| = 1$ change, which produces the stabilized *Ms* = ±1/2 components, leads to a positive contribution to the *D* value.[69] The relative energy order (cm^{-1}) of ligand field d-orbitals splitting for complexes **1**-**2** have been extracted according to *ab initio* ligand field theory (AILFT)[86] analysis using NEVPT2 implemented in ORCA 4.2 (Table S9, ESI†). Molecular coordination frame was chosen in such a way that *Z* axis goes along the numerically largest eigenvalue of the *D*-tensor and the *X* and *Y* axis accordingly to the other two (Figure S10). The following discussion of Co(II) *d*-atomic orbitals (*d*-AOs) are classified in accordance with this frame. The orbital energies computed for the ground state of **1**-**2** are shown in Fig. S11.

For **1** and **2**, the most destabilized by ligand field is the singly occupied orbital composed of practically pure d_{z2} AOs. The orbital energies computed for the ground states are shown in Figure S11, where the ground states for **1** and **2** are both multideterminant with prevailing (73.7% and 70.2%, respectively) contribution of $(d_{yz})^1(d_{xz})^2(d_{xy})^1(d_{x2-y2})^2(d_{z2})^1$ and $(d_{yz})^1(d_{xz})^2(d_{xy})^1(d_{x2-y2})^2(d_{z2})^1$, and are mixed with another with the weightage of 10.0% and 10.7%, respectively. For **1**, the major contribution to *D* is from the ground to the second excited state transition (d_{xz}→d_{xy}, Figure S11 and S12). The positive sign of the *D* parameter is attributed to these transitions, which occur between orbitals with the different magnetic quantum number (m_l) values.[17, 87] In the case of **2**, the largest contribution to *D* is also from the ground to the second excited state transition (d_{xz}→d_{xy}, Figure S11 and S12). Since these orbitals also have different m_l value, the contribution to the *D* value is positive.[17, 86]

The multideterminantal wavefunctions of the selected excited states having important contributions to *D* tensor are shown in Fig. S14, where all of the excited states of **1** and **2** are composed of several configurations indicating the presence of the unquenched orbital angular momentum. The calculated $\chi_M T$ versus *T* plots of complexes **1** and **2** are shown in Fig. S13. The calculated orientations of the g_x, g_y and g_z in the ground spin-orbit states on Co(II) ions of **1** and **2** are shown in Fig. S14.

Conclusions

In summary, the magnetic anisotropy and slow magnetic dynamics of two four-coordinate mononuclear Co(II) complexes **1** and **2** with the $[CoPX_3]^-$ moiety have been studied. Their positive magnetic anisotropies have been demonstrated by magnetometry, HF-EPR and theoretical calculations. As in the cases of other reported four-coordinate Co(II)-SIMs with a mixed donor set from N, P, As, O, S, Se and/or halides, the ac susceptibility studies demonstrate that **1** and **2** exhibit slow magnetic relaxation behavior under the applied dc fields. In comparison, zero-field slow magnetic relaxation has been observed in some homoleptic SIMs containing a CoX_4 unit (X = O,[44] S,[45] Se,[44] Te,[46] N[47]) with four identical donors, but not in

those with X = Cl^-.[48] Such observations suggest that the homoleptic four-coordinate Co(II) complexes prefer to exhibit magnetic relaxation under zero-field than those heteroleptic complexes.

Compared with the reported Co(II)-SIMs with the $CoAB_3$ moiety, complexes **1** and **2** have two important features. Firstly, they contain phosphorus atoms, which is rare for the four-coordinate Co(II)-SIMs since most of them are coordinated by nitrogen-containing ligands (Table S1). Secondly, molecules of both **1** and **2** exhibit distorted tetrahedral geometry with crystallographically imposed C_{3v} symmetry. Considering both complexes possess large and positive magnetic anisotropy, these results further support that coordination environment and symmetry have significant impact on the magnetic properties of Co(II) complexes.

Conflicts of interest

There are no conflicts to declare.

Acknowledgements

We are grateful for the financial support from the National Natural Science Foundation of China (No. 21471078 to XTC and 21973046 to YQZ), the Joint Fund for Regional Innovation and Development (U20A2073 to ZWO and ZW), and the US National Science Foundation (CHE-1900296 and CHE-2055499 to ZLX).

Notes and references

1 R. Bagai and G. Christou, *Chem. Soc. Rev.*, 2009, 38, 1011-1026.
2 K. S. Pedersen, J. Bendix and R. Clerac, *Chem. Commun.*, 2014, **50**, 4396-415.
3 W. Wernsdorfer and R. Sessoli, *Science*, 2009, **284**, 133-135.
4 M. N. Leuenberger and D. Loss, *Nature*, 2001, **410**, 789-793.
5 M. Affronte, *J. Mater. Chem.*, 2009, **19**, 1731-1737.
6 F. Neese and D. A. Pantazis, *Faraday Discuss.*, 2011, **148**, 229-238.
7 N. Ishikawa, M. Sugita, T. Ishikawa, S. Koshihara and Y. Kaizu, *J. Am. Chem. Soc.*, 2003, **125**, 8694-8695.
8 D. N. Woodruff, R. E. P. Winpenny and R. A. Layfield, *Chem. Rev.*, 2013, **113**, 5110-5148.
9 J. M. Frost, K. L. M. Harriman and M. Murugesu, *Chem. Sci.*, 2016, **7**, 2470-2491.
10 G. A. Craig and M. Murrie, *Chem. Soc. Rev.*, 2015, **44**, 2135-2147.
11 A. K. Bar, C. Pichon and J.-P. Sutter, *Coord. Chem. Rev.*, 2016, **308**, 346-380.
12 J. Vallejo, I. Castro, R. Ruiz-Garcia, J. Cano, M. Julve, F. Lloret, G. De Munno, W. Wernsdorfer and E. Pardo, *J. Am. Chem. Soc.*, 2012, **134**, 15704-7.
13 Y.-Z. Zhang, S. Gomez-Coca, A. J. Brown, M, R. Saber, X. Zhang and K. R. Dunbar, *Chem. Sci.*, 2016, **7**, 6519-6527.
14 J. M. Zadrozny and J. R. Long, *J. Am. Chem. Soc.*, 2011, **133**, 20732-20734.
15 A. Eichhöfer, Y.-H. Lan, V. Mereacre, T. Bodenstein and F. Weigend, *Inorg. Chem.*, 2014, **53**, 1962-1974.
16 A. M. Bryan, G. J. Long, F. Grandjean and P. P. Power, *Inorg. Chem.*, 2013, **52**, 12152-12160.
17 S. Gomez-Coca, E. Cremades, N. Aliaga-Alcalde and E. Ruiz, *J. Am. Chem. Soc.*, 2013, **135**, 7010-7018.
18 Y.-Y. Zhu, C. Cui,Y.-Q. Zhang, J.-H. Jia, X. Guo, C. Gao, K. Qian, S.-D. Jiang, B.-W. Wang, Z.-M. Wang and S. Gao, *Chem. Sci*., 2013, **4**, 1802-1806.
19 M. R. Saber, M.K. Singh and K.R. Dunbar, *Chem. Commun.*, 2020. **56**, 8492-8495.
20 J. Vallejo, E. Pardo, M. Viciano-Chumillas, I. Castro, P. Amoros, M. Deniz, C. Ruiz-Perez, C. Yuste-Vivas, J. Krzystek, M. Julve, F. Lloret and J. Cano, *Chem. Sci.*, 2017, **8**, 3694-3702.
21 T. Ishizaki, T. Fukuda, M. Akaki, A. Fuyuhiro, M. Hagiwara and N. Ishikawa, *Inorg. Chem.*, 2019, **58**, 5211-5220.
22 D. Pinkowicz, F. J. Birk, M. Magott, K. Schulte and K. R. Dunbar, *Chem. Eur. J.*, 2017, **23**, 3548-3552.
23 K. A. Schulte, K. R. Vignesh and K. R. Dunbar, *Chem. Sci.*, 2018, **9**, 9018-9026.
24 S. Ziegenbalg, D. Hornig, H. Gorls and W. Plass, *Inorg. Chem.*, 2016, **55**, 4047-58.
25 A. A. Garcia-Valdivia, J. M. Seco, J. Cepeda and A. Rodriguez-Dieguez, *Inorg. Chem.*, 2017, **56**, 13897-13912.
26 G. Peng, Y. Chen, B. Li, Y.-Q. Zhang and X.-M. Ren, *Dalton Trans.*, 2020, **49**, 5798-5802.
27 D. Kowalkowska-Zedler, A. Dolega, N. Nedelko, R. Lyszczek, P. Aleshkevych, I. Demchenko, J. Luczak, A. Slawska-Waniewska and A. Pladzyk, *Dalton Trans.*, 2020, **49**, 697-710.
28 A. M. Majcher, P. Dabczynski, M. M. Marzec, M. Ceglarska, J. Rysz, A. Bernasik, S. I. Ohkoshi and O. Stefanczyk, *Chem. Sci.*, 2018, **9**, 7277-7286.
29 M. Ceglarska, O. Stefanczyk, S. I. Ohkoshi and A.-M. Majcher, *Dalton Trans.*, 2020, **49**, 6807-6815.
30 F. Yang, Q. Zhou, Y. Zhang, G. Zeng, G. Li, Z. Shi, B. Wang and S. Feng, *Chem. Commun.*, 2013, **49**, 5289-91.
31 R. Boča, J. Miklovič and J. Titiš, *Inorg. Chem.*, 2014, **53**, 2367-2369.
32 M. R. Saber and K. R. Dunbar, *Chem. Commun*., 2014, **50**, 12266-9.
33 C. Rajnák, A. Packová, J. Titiš, J. Miklovič, J. Moncol' and R. Boča, *Polyhedron*, 2016, **110**, 85-92.
34 Y.-Q. Zhai, Y.-F. Deng and Y.-Z. Zheng, *Dalton Trans.*, 2018, **47**, 8874-8878.
35 A. K. Mondal, M. Sundararajan and S. Konar, *Dalton Trans*, 2018, **47**, 3745-3754.
36 J. Hruby, D. Dvorak, L. Squillantini, M. Mannini, J. van Slageren, R. Herchel, I. Nemec and P. Neugebauer, *Dalton Trans.*, 2020, **49**, 11697-11707.
37 A. N. Bone, C. N. Widener, D. H. Moseley, Z. Liu, Z. Lu, Y. Cheng, L. L. Daemen, M. Ozerov, J. Telser, K. Thirunavukkuarasu, D. Smirnov, S. M. Greer, S. Hill, J. Krzystek, K. Holldack, A. Aliabadi, A. Schnegg, K. R. Dunbar, Z.-L. Xue, *Chem. Eur. J.*, 2021, **27**, 11110–11125.
38 R.-C. Yang, D.-R. Wang, J.-L. Liu, Y.-F. Wang, W.-Q. Lin, J.-D. Leng and A.-J. Zhou. *Chem. Asian J.*, 2019, **14**,1467-1471.
39 S. Vaidya, S. K. Singh, P. Shukla, K. Ansari, G. Rajaraman and M. Shanmugam, *Chem. Eur. J.*, 2017, **23**, 9546-9559.
40 S. Vaidya, P. Shukla, S. Tripathi, E. Riviere, T. Mallah, G. Rajaraman and M. Shanmugam, *Inorg. Chem.*, 2018, **57**, 3371-3386.
41 M. R. Saber, J. A. Przyojski, Z. J. Tonzetich and K. R. Dunbar, *Dalton Trans.*, 2020, **49**, 11577-11582.
42 J. M. Zadrozny, J. Liu, N. A. Piro, C. J. Chang, S. Hill and J. R. Long, *Chem. Commun.*, 2012, **48**, 3927-9.
43 O. Y. Vassilyeva, E. A. Buvaylo, V. N. Kokozay, B. W. Skelton, C. Rajnak, J. Titis and R. Boca, *Dalton Trans.*, 2019, **48**, 11278-11284.
44 J. M. Zadrozny, J. Telser and J. R. Long, *Polyhedron*, 2013, **64**, 209-217.

45 J. M. Zadrozny and J. R. Long, *J. Am. Chem. Soc.*, 2011, **133**, 20732-20734.
46 X.-N. Yao, M.-W. Yang, J. Xiong, J.-J. Liu, C. Gao, Y.-S. Meng, S.-D. Jiang, B.-W. Wang and S. Gao, *Inorg. Chem. Front.* 2017, **4**, 701-705.
47 Y. Rechkemmer, F. D. Breitgoff, M. van der Meer, M. Atanasov, M. Hakl, M. Orlita, P. Neugebauer, F. Neese, B. Sarkar and J. van Slageren, *Nat. Commun.*, 2016, **7**, 10467.
48 A. Piecha-Bisiorek, A. Bienko, R. Jakubas, R. Boca, M. Weselski, V. Kinzhybalo, A. Pietraszko, M. Wojciechowska, W. Medycki and D. Kruk, *J. Phys. Chem. A*, 2016, **120**, 2014-21.
49 F. A. Cotton, O. D. Faut, D. M. L. Goodgame and R. H. Holm, *J. Am. Chem. Soc.*, 1961, **83**, 1780-1785.
50 *SMART & SAINT Software Reference Manuals, version 6.45,* Bruker Analytical X-ray Systems, Inc., Madison, WI, 2003.
51 SAINT, *Program for Data Extraction and Reduction,* Siemens Analytical X-ray Instruments, Madison, WI, 1994 - 1996.
52 G. M. Sheldrick, *SADABS: Software for Empirical Absorption Correction, version 2.05,* University of Göttingen: Göttingen, Germany, 2002.
53 G. M. Sheldrick, *Acta Crystallogr. Sect. C: Struct. Chem.*, 2015, **71**, 3.
54 G. A. Brain and J. F. Berry, *J. Chem. Educ.*, 2008, **85**, 532-536.
55 S.-L. Wang, L. Li, Z.-W. Ouyang, Z.-C. Xia, N. M. Xia, T. Peng and K.-B. Zhang, *Acta Phys. Sin.*, 2012. **61**, 107610.
56 H. Nojiri and Z.-W. Ouyang, *Terahertz Sci. Technol.*, 2012. **5**, 10.
57 G.-Q. Li, F.-Q. Zheng, G.-C. Guo and J.-S. Huang, *Chin. J. Struct. Chem*, 2000, **19**, 230-233.
58 D. Fenske, R. Basoglu, J. Hachgenei and F. Rogel, *Angew. Chem. Int. Ed. Engl.*, 1984, **23**, 160.
59 A. Romerosa, C. Saraiba-Bello, M. Serrano-Ruiz, A. Caneschi, V. Mckee, M. Peruzzini, L. Sorace and F. Zanobini, *Dalton Trans.*, 2003, **16**, 3233-3239.
60 C. E. Kriley, M. M. Majireck, J. M. Tobolewski, L. E. Kelvington, S. H. Cummings, S. J. Hershberger, J. D. Link, A. L. Silverio, P. E. Fanwick and I. P. Rothwell, *Inorg. Chim. Acta*, 2005, **358**, 57-62.
61 G. A. Seisenbaeva, V. G. Kessler, R. Pazik and W. Strek, *Dalton Trans.*, 2008, **26**, 3412-21.
62 S. Jie, M. Agostinho, A. Kermagoret, C. S. Casin and P. Braunstein, *Dalton Trans.*, 2007, **39**, 4472-4482.
63 G. Kiefer, H. Vrubel, R. Scopelliti and K. Severin, Eur. *J. Inorg. Chem.*, 2013, 4916-4921.
64 M. W. Drover, K. Nagata and J. C. Peters, *Chem. Commun.*, 2018, **54**, 7916-7919.
65 S. Alvarez, P. Alemany, D. Casanova, J. Cirera, M. Llumell and D. Avnir, *Coord. Chem. Rev.*, 2005. **249**, 1693-1708.
66 M. Llunell, D. Casanova, J. Ciera, P. Alemany and S. Alvarez, *Shape Program 2013 Vision 2.1.*
67 N. F. Chilton, R, P. Anderson, L. D. Turner, A. Soncini and K. S. Murray, *J. Comput. Chem.*, 2013, **34**, 1164-75.
68 Simulations were performed using SPIN developed by Andrew Ozarowski of the National High Magnetic Field Laboratory, USA.
69 K. S. Cole and R. H. Cole, *J. Chem. Phys.*, 1941, **9**, 341-351.
70 Y.-N. Guo, G.-F. Xu, Y. Guo and J. Tang, *Dalton Trans.*, 2011, **40**, 9953-9963.
71 A. Singh and K. N. Shrivasta, *Phys. Stat. Sol. (b)*, 1979, **95**, 273.
72 K. N. Shrivastava, *Phys. Stat. Sol. (b)*, 1983, **117**, 437-458.
73 P. L. Scott and C. D. Jeffries, *Phys. Rev.*, 1962, **127**, 32-51.
74 R. Ishikawa, Y. Horii, R. Nakanishi, S. Ueno, B. K. Breedlove, M. Yamashita and S. Kawata, *Eur. J. Inorg. Chem.* 2016, 3233–3239.
75 R. Mitsuhashi, S. Hosoya, T. Suzuki, Y. Sunatsuki, H. Sakiyama and M. Mikuriya, *Dalton Trans.*, 2019, **48**, 395–399.
76 T. T. da Cunha, V. M. M. Barbosa, W. X. C. Oliveira, E. F. Pedroso, D. M. A. García, W. C. Nunes and C. L. M. Pereira, *Inorg. Chem.*, 2020, **59**, 12983−12987.
77 R.Mitsuhashi, K. S. Pedersen, T. Ueda, T. Suzuki, J. Bendix and M. Mikuriya, *Chem. Commun.*, 2018, **54**, 8869-8872.
78 K. Hchicha, M. Korb, A. Kliuikov, E. Čižmár and H. Naïli, *J. Magn. Magn. Mater.*, 2021, **536**, 168140(1-13).
79 A. Świtlicka, B. Machura, A. Bieńko, S. Kozieł, D. C. Bieńko, C. Rajnák, R. Boča, A. Ozarowski and M. Ozerov, *Inorg. Chem. Front.*, 2021, **8**, 4356–4366.
80 P. Zoufaly, A. Kliuikov, E. Čižmár, I. Císařová and R. Herchel, *Eur. J. Inorg. Chem.* 2021, 1190–1199.
81 C. Benniston, S. Melnic, C. Turta, A. B. Arauzo, J. Bartolomé, E. Bartolomé, R. W. Harrington and M. R. Probert, *Dalton Trans.*, 2014, **43**, 13349–13357.
82 K. Uchida, G. Cosquer, K. Sugisaki, H. Matsuoka, K. Sato, B. K. Breedlove and M. Yamashita, *Dalton Trans.*, 2019, **48**, 12023–12030.
83 W.-Q. Lin, T. Bodenstein, V. Mereacre, K. Fink and A. Eichhöfer, *Inorg. Chem.* 2016, **55**, 2091−2100.
84 F. Aquilante, J. Autschbach, R. K. Carlson, L. F. Chibotaru, M. G. Delcey, L. De Vico, I. Fdez Galván, N. Ferré, L. M. Frutos, L. Gagliardi, M. Garavelli, A. Giussani, C. E. Hoyer, G. Li Manni, H. Lischka, D. Ma, P. Å. Malmqvist, T. Müller, A. Nenov, M. Olivucci, T. B. Pedersen, D. Peng, F. Plasser, B. Pritchard, M. Reiher, I. Rivalta, I. Schapiro, J. Segarra-Martí, M. Stenrup, D. G. Truhlar, L. Ungur, A. Valentini, S. Vancoillie, V. Veryazov, V. P. Vysotskiy, O. Weingart, F. Zapata, R. Lindh, *J. Comput. Chem.*, 2016, **37**, 506-541.
85 F. Neese, *ORCA - an ab initio, density functional and semiempirical program package,* Max-Plank institute for bioinorganic chemistry, Mülheim an der Ruhr, Germany, 2019.
86 M. Atanasov, D. Ganyushin, K. Sivalingam and F. Neese, *in Molecular Electronic Structures of Transition Metal Complexes II.* eds. D. M. P. Mingos, P. Day and J. P. Dahl, Springer Berlin Heidelberg, Berlin, Heidelberg, 2012.
87 S. Gómez-Coca, D. Aravena, R. Morales and E. Ruiz, *Coord. Chem. Rev.*, 2015, **289-290**, 379-392.

Magnetic anisotropy of two tetrahedral Co(II)-halide complexes with triphenylphosphine ligands

Wei Lv,[a] Hui-Hui Cui,[a] Lei Chen,[b] Yi-Quan Zhang,*[c] Xue-Tai Chen,*[a] Zhenxing Wang,*[d] Zhong-Wen Ouyang[d] and Zi-Ling Xue[e]

[a]*State Key Laboratory of Coordination Chemistry, School of Chemistry and Chemical Engineering, Nanjing University, Nanjing 210023, China*

[b]*School of Environmental and Chemical Engineering, Jiangsu University of Science and Technology, Zhenjiang 212003, China*

[c]*Jiangsu Key Laboratory for NSLSCS, School of Physical Science and Technology, Nanjing Normal University, Nanjing 210023, China*

[d]*Wuhan National High Magnetic Field Center & School of Physics, Huazhong University of Science and Technology, Wuhan 430074, China*

[e]*Department of Chemistry, University of Tennessee, Knoxville, Tennessee 37996, USA*

Electronic Supplementary Information

Table S1 Complexes with $[CoAB_3]$ moiety and their structure/magnetic parameters

Complex[a]	Coordination moiety	D/cm^{-1}	$\|E\|$/cm^{-1}	U_{eff} / K[b]	Reference
1	$[CoPCl_3]$	+42.8	0	c	This work
2	$[CoPBr_3]$	+41.2	0	c	This work
$[Co(L^1)Cl_3]$ (**3**)	$[CoNCl_3]$	+19.9	3.37	d	18
$[(L^2)CoCl]^+$ **(4)**	$[CoN_3Cl]$	+12.7	1.2	34.5 (1500 Oe)	19
$K[Co(L^3)]$ **(5)**	$[CoNN'_3]$	+33	0.2	45 (1000 Oe)	20
$[Co(L^4)]$ **(6)**	$[CoNN'_3]$	+16	0.0	12.5 (1500 Oe)	21
$[LiTHF][Co(L^5)]$ **(7)**	$[CoNN'_3]$	+27	4.0	26 (1000 Oe)	22

a. Ligands: L^1 = 2-methyl-3-(pyridin-2-yl)imidazo[1,5-a]pyridinium cation; $L^2 = CH_3C[CH_2N{=}CN(CH_3)_2]_3$; L^3 = N,N',N''-[nitrilotris-(ethane-2,1-diyl)]tris(2,4,6-trimethylbenzenesulfonamide); $L^4 = N[CH_2C(O)NC(CH_3)_3]_3$; $L^5 = [(Me_3SiNCH_2CH_2)_3N]^{3-}$. b. The applied field used in the measurement is indicated in the parenthesis. c. No Orbach mechanism is found. d. Not reported.

Table S2 Complexes with $[CoP_2X_2]$ moiety and their structure/magnetic parameters

Complex	Coordination moiety	D /cm^{-1}	$\|E\|$ /cm^{-1}	U_{eff} / K[c]	Reference
$[Co(PPh_3)_2Cl_2]$ **(8)**	$[CoP_2Cl_2]$	-16.2	0.9	37.1 (1000 Oe)	23
$[Co(L^6)Cl_2]$ **(9)**	$[CoP_2Cl_2]$	-14.4	1.7	35.0 (1000 Oe)	23
$[Co(L^7)Cl_2]$ **(10)**	$[CoP_2Cl_2]$	-15.4	1.3	29.9 (1000 Oe)	23
$[Co(PPh_3)_2Br_2]$ **(11)**	$[CoP_2Br_2]$	-13	--	37 (1000 Oe)	24
$[Co(PPh_3)_2I_2]$ (**12**)	$[CoP_2I_2]$	-36.9	0.2	30.6 (1000 Oe)	25
$[Co(PPh_3)_2(NCS)_2]$(**13**)	$[CoP_2N_2]$	-9.44	1.60	b	26
$[Co(L^8)(NCS)_2]$ **(14)**	$[CoP_2N_2]$	-11.4	0.46	31.8 (3000 Oe)	27
$[Co(L^9)(NCS)_2]$ **(15)**	$[CoP_2N_2]$	-16.2	1.1	30.1 (1000 Oe)	28
$[Co(L^9)Cl_2]$ **(16)**	$[CoP_2Cl_2]$	-15.1	0.9	25.5 (1000 Oe)	28
$[Co(L^9)Br_2]$ **(17)**	$[CoP_2Br_2]$	-11.6	1.2	18.7 (1000 Oe)	28
$[Co(L^9)I_2]$ **(18)**	$[CoP_2I_2]$	-7.3	1.5	9.2 (1000 Oe)	28
$[CoCl_2(dppf)]$ **(19)**	$[CoP_2Cl_2]$	-11.0	0	33.3 (1000 Oe)	29
$[CoBr_2(dppf)]$ **(20)**	$[CoP_2Br_2]$	-8.7	2.09	28.8 (1000 Oe)	29

a. Ligands: L^6 = DPEphos = 2,2'-bis(diphenyl-phosphino) diphenyl ether; L^7 = Xantphos = 9,9-dimethyl-4,5-bis(diphenyl-phosphino) xanthenes; L^8 = bis(2-(diphenylphosphaneyl)-4-methylphenyl)amine; L^9 = 9,9-dimethyl-4,5-bis(diphenylphosphino)xanthenes; dppf = 1,1′-ferrocenediyl-bis(diphenylphosphine). b. Not reported. c. The applied field used in the measurement is indicated in the parenthesis.

Table S3 Summary of crystal data and refinement for **1** and **2**

	1	**2**
Molecular formula	$C_{26}H_{35}NPCl_3Co$	$C_{26}H_{35}NPBr_3Co$
CCDC no	2074688	2074732
Formula weight	557.80	691.18
Temperature/K	296(2)	296(2)
Crystal system	Cubic	Cubic
Space group	$Pa\bar{3}$	$Pa\bar{3}$
a / Å	17.5892(2)	17.86950(10)
b / Å	17.5892(2)	17.86950(10)
c / Å	17.5892(2)	17.86950(10)
α (°)	90	90
β (°)	90	90
γ (°)	90	90
V / Å^3	5441.75(19)	5706.17(10)
Z	8	8
D_{calc}, g/cm^3	1.362	1.609
μ / mm^{-1}	0.999	4.873
F (000)	2328.0	2760.0
θ range [°]	2.005/25.977	1.974/25.974
Reflns collected	42768	45367
R_{int}	0.0574	0.0608
Indep. reflns	1795	1869
Data/restr./paras	1795/215/149	1869/203/149
Goodness-of-fit on F^2	1.064	1.094
R_1, wR_2 [$I > 2\sigma(I)$][a]	0.0600/0.1565	0.0750/0.1755
R_1, wR_2 [all data][a]	0.0740/0.1700	0.0946/0.1889

[a]$wR_2 = [\Sigma[w(F_o^2–F_c^2)^2]/\Sigma[w(Fo^2)^2]]^{1/2}$, $R_1 = \Sigma||F_o|–|F_c||/\Sigma|F_o|$.

Table S4 Selected bond lengths (Angstroms) and angels (degree) for **1** and **2**

1		**2**	
Co1-P1	2.3763(16)	Co1-P1	2.373(3)
Co1-Cl1	2.2508(12)	Co1-Br1	2.3827(10)
Cl1-Co1-Cl1	114.11(4)	Br1-Co1-Br1	113.39(4)
P1-Co1-Cl1	104.30(5)	P1-Co1-Br1	105.19(5)

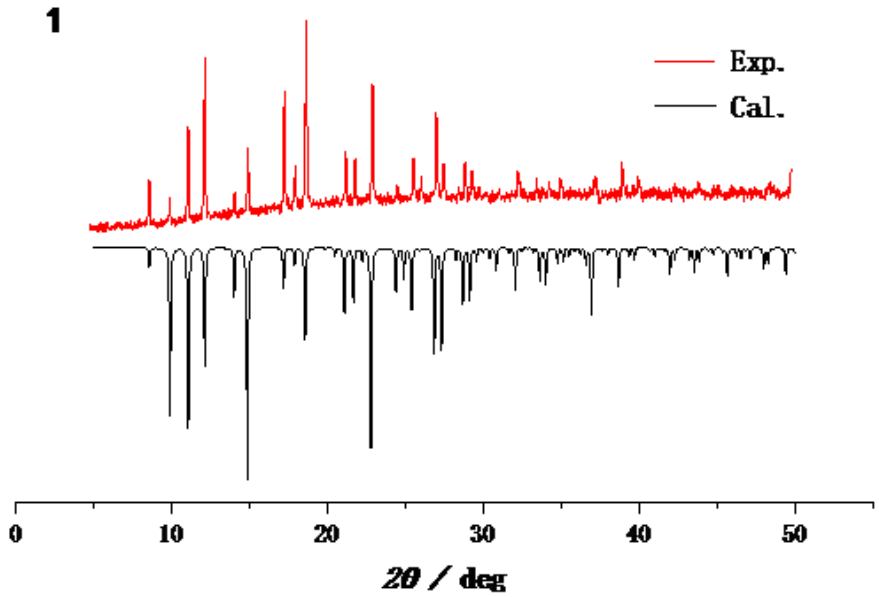

Fig. S1 XRD patterns for **1** (The red line are PXRD experimental pattern and the black line are calculated from single-crystal structure)

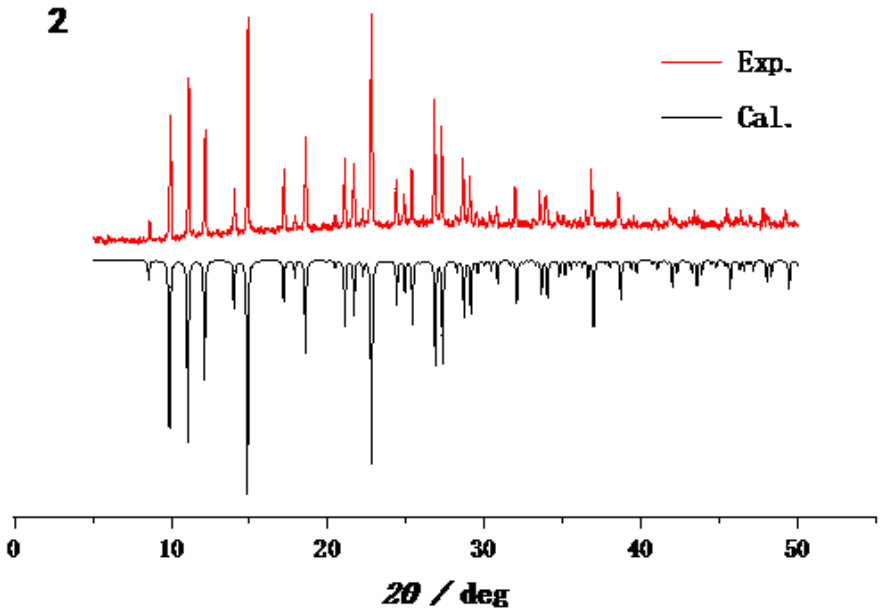

Fig. S2 XRD patterns for complex **2** (The red line are PXRD experimental pattern and the black line are calculated from single-crystal structure).

Table S4 The results of the continuous shape measure (*CShM*) analyses of **1** and **2** by SHAPE software.[1, 2]

Four-vertex	Deviation parameter			
	Square	Tetrahedron	Seesaw	Vacant trigonal bipyramid
1	33.432	0.177	8.903	2.258
2	33.417	0.199	8.889	2.112

PHI survey plots: In oder to check the accuracy of the set of the fitted parameters, survey features have been performed using the PHI code.[3] Among the three parameters D, $g_x(g_y)$ and g_z, one parameter was fixed and the other two are varied. All the survey plots show that the fitted parameters are in the narrow minimum regions.

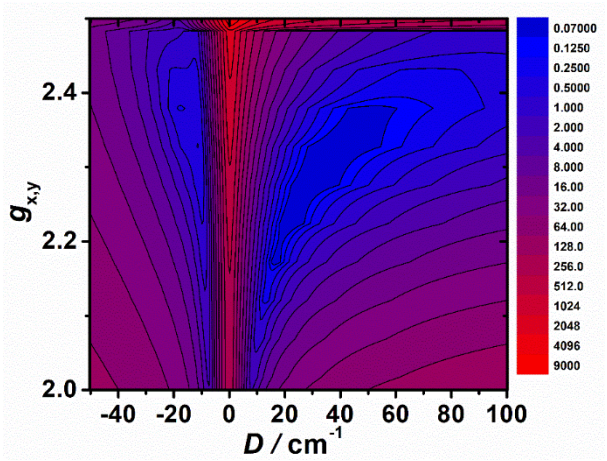

(a)

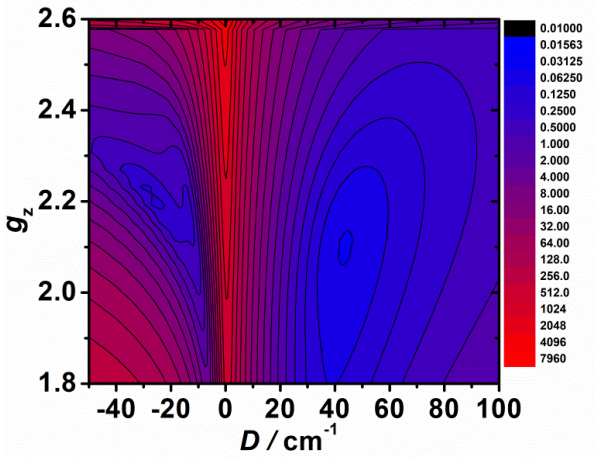

(b)

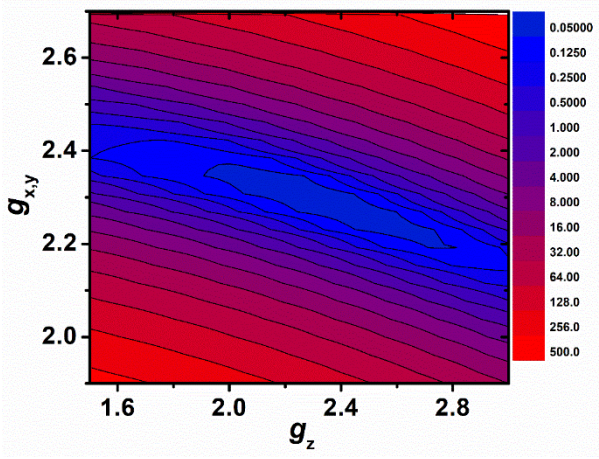

(c)

Fig. S3 The survey plots of complex **1**: (a) g_z was fixed as 2.103; (b) $g_x(g_y)$ was fixed as 2.236 and (c) D was fixed as 42.8 cm^{-1}.

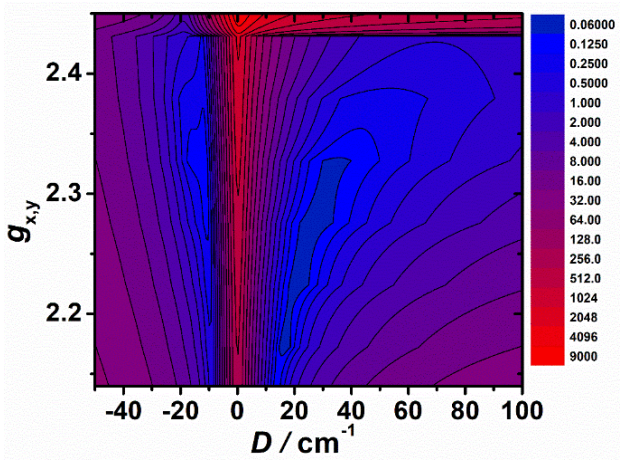

(a)

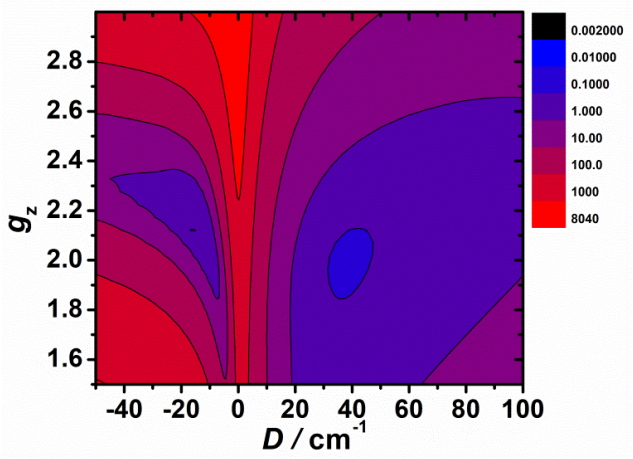

(b)

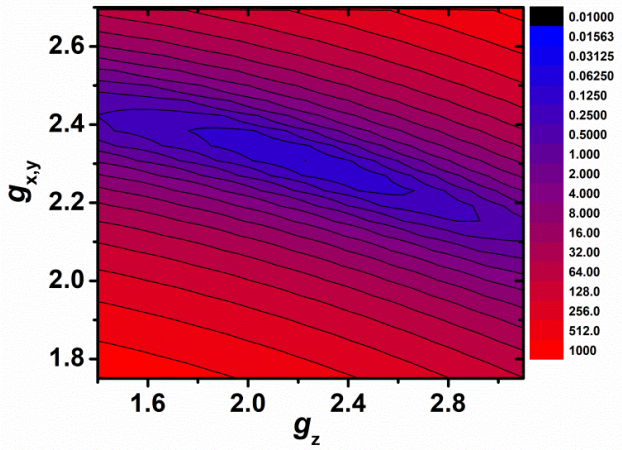

(c)

Fig. S4 The survey plots of complex **2**: (a) g_z was fixed as 2.136; (b) $g_x(g_y)$ was fixed as 2.262 and (c) D was fixed as 41.2 cm^{-1}.

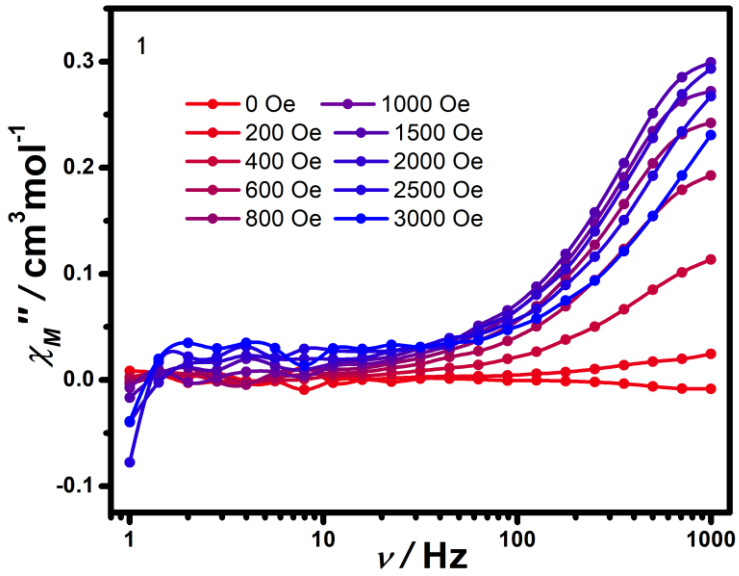

(a)

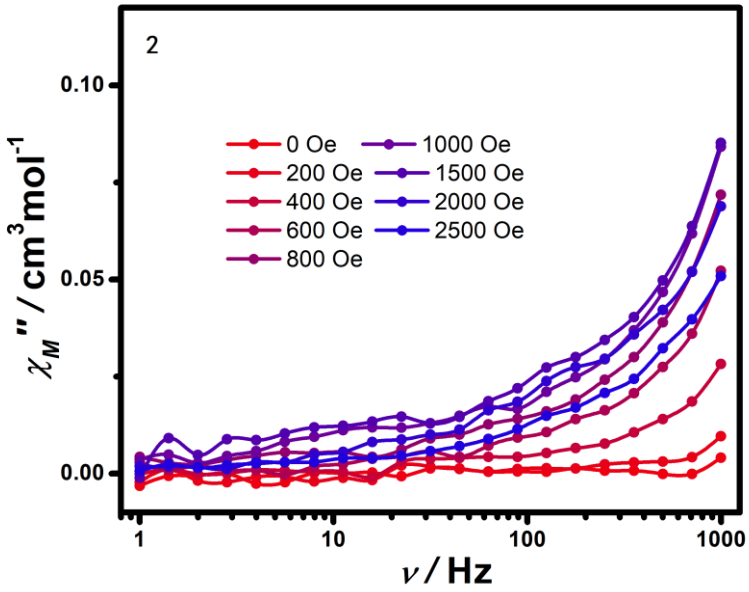

(b)

Fig. S5 Frequency dependence of out-of-phase ac susceptibility (χ_M'') at 1.8 K under the different applied static fields from 0 to 0.25 T for **1** (a) and **2** (b). The solid lines are for eye guide.

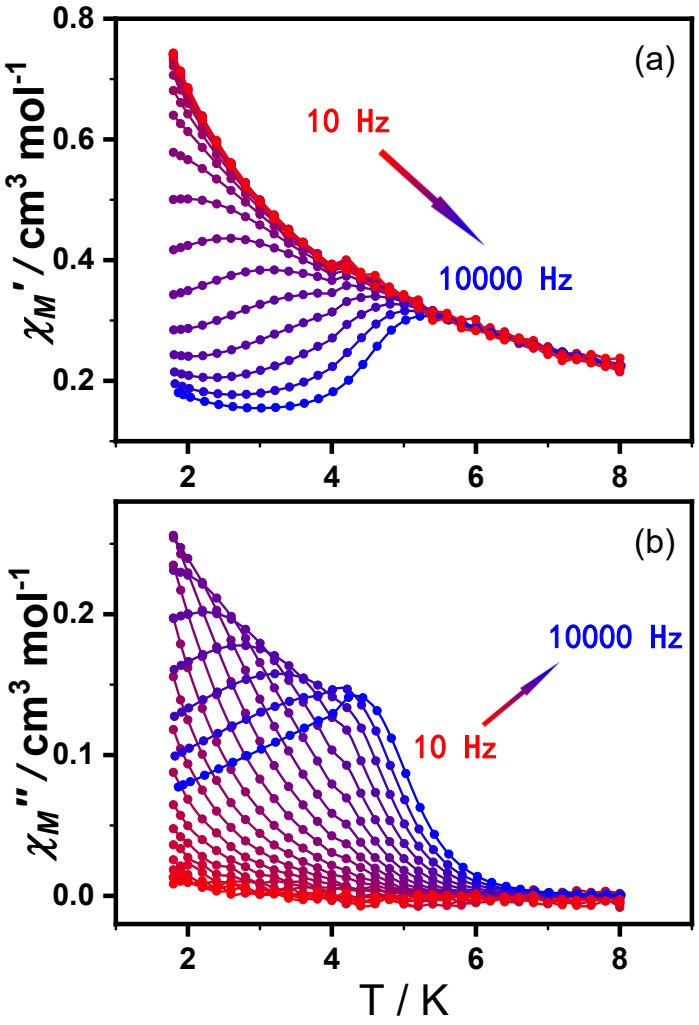

Fig. S6 Temperature dependence of (a) in-phase (χ_M') and (b) out-of-phase ac susceptibility (χ_M'') at different ac frequencies under the dc field of 0.12 T for **1**. The solid lines are for eye guide.

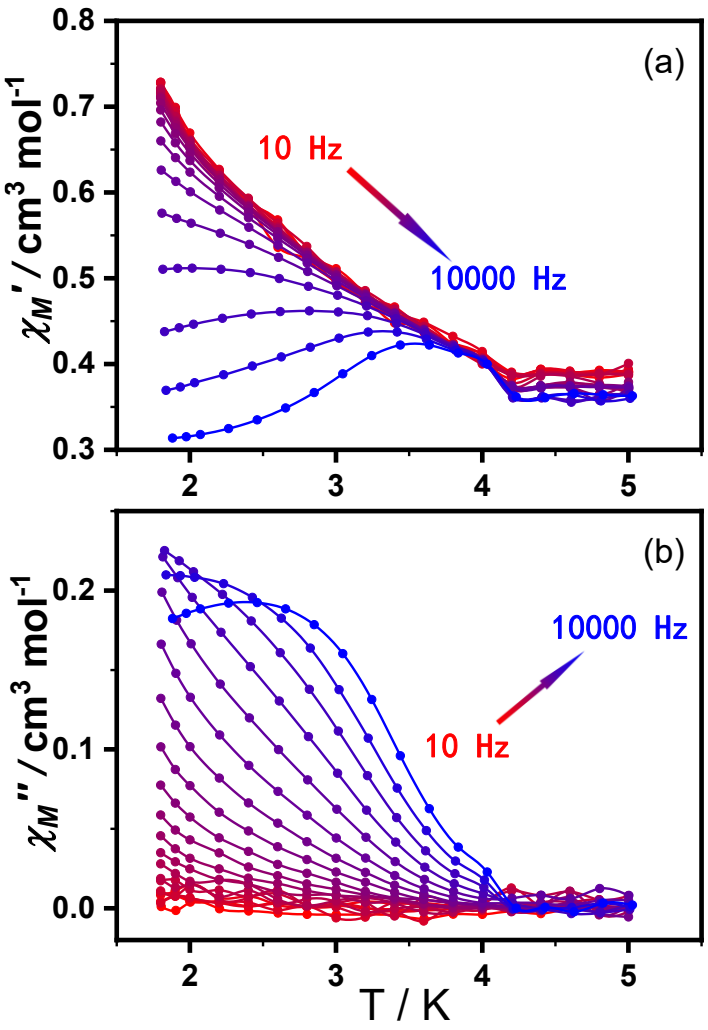

Fig. S7 Temperature dependence of (a) in-phase (χ_M') and (b) out-of-phase ac susceptibility (χ_M'') at different ac frequencies under the dc field of 0.15 T for **2**. The solid lines are for eye guide.

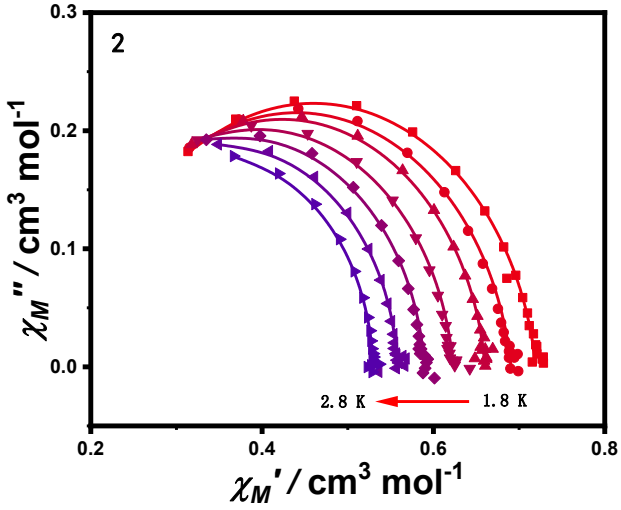

Fig. S8 Cole−Cole plots for **2** under 0.15 T dc field. The solid lines are the best fits to the experiments with the generalized Debye model.

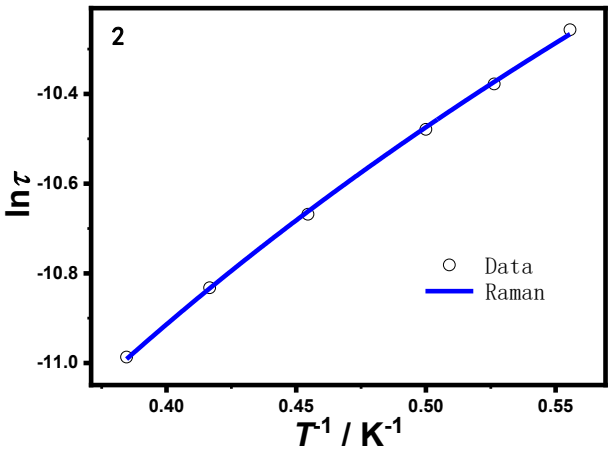

Fig. S9 The plot of ln(τ) versus T^{-1} for **2**. The solid blue line represents the best fit by the Raman process.

Table S5 Relaxation times τ (s) and α values for **1** and **2**

1				
T (K)	χ_S	χ_T	τ (s)	α
1.8	0.16775	0.7448	1.46616×10^{-4}	0.07053
1.9	0.16128	0.71303	1.33689×10^{-4}	0.0677
2.0	0.1559	0.68453	1.22337×10^{-4}	0.0625
2.2	0.15031	0.66035	1.1247×10^{-4}	0.06088
2.4	0.14531	0.63827	1.03745×10^{-4}	0.05875
2.6	0.14109	0.61614	9.56154×10^{-5}	0.05418
2.8	0.13704	0.5963	8.83302×10^{-5}	0.05117
3.0	0.13348	0.57683	8.16139×10^{-5}	0.04658
3.2	0.12929	0.55981	7.55874×10^{-5}	0.04619
3.4	0.1259	0.5438	7.01833×10^{-5}	0.04433
3.6	0.12413	0.52708	6.51943×10^{-5}	0.03701
3.8	0.12039	0.51323	6.06515×10^{-5}	0.03822
4.0	0.11787	0.49878	5.6357×10^{-5}	0.03462
4.4	0.11575	0.48508	5.2464×10^{-5}	0.03065
4.8	0.11296	0.47285	4.88591×10^{-5}	0.03029
5.2	0.11133	0.45994	4.54591×10^{-5}	0.02472
5.6	0.10949	0.44831	4.23382×10^{-5}	0.02156
6.0	0.10701	0.43822	3.93648×10^{-5}	0.02217
6.4	0.10504	0.42854	3.65816×10^{-5}	0.02144
6.8	0.1026	0.4181	3.37456×10^{-5}	0.01988
7.2	0.1023	0.40843	3.12653×10^{-5}	0.01367
7.6	0.1009	0.39929	2.87198×10^{-5}	0.01058
8.0	0.09871	0.39092	2.61773×10^{-5}	0.01048
2				
T (K)	χ_S	χ_T	τ (s)	α

1.8	0.20105	0.71947	3.51115×10^{-5}	0.08591
1.9	0.18959	0.6906	3.11135×10^{-5}	0.08737
2.0	0.18673	0.66015	2.81235×10^{-5}	0.06759
2.2	0.16967	0.62287	2.32724×10^{-5}	0.06667
2.4	0.16144	0.58927	1.97552×10^{-5}	0.05378
2.6	0.15936	0.5578	1.69242×10^{-5}	0.03441
2.8	0.15789	0.52916	1.41798×10^{-5}	0.01963
3.0	0.14601	0.50458	1.08899×10^{-5}	0.02683
3.2	0.14768	0.48031	8.20644×10^{-6}	0.01659
3.4	0.16043	0.45787	6.05389×10^{-6}	8.27505×10^{-4}
3.6	0.22726	0.44122	5.30153×10^{-6}	0.00112
4.0	0.00937	0.4237	1.14426×10^{-6}	0.11771
4.2	1.98419×10^{-7}	0.40805	3.95027×10^{-7}	0.23328
4.4	3.04973×10^{-7}	0.39081	1.97231×10-7	0.24095
4.6	1.94707×10^{-6}	0.37507	1.37693×10^{-7}	0.19865
4.8	9.15375×10^{-6}	0.36211	2.40381×10^{-8}	0.34942
5.0	1.77633×10^{-5}	0.34628	1.55948×10^{-7}	7.46318×10^{-9}

Compoutation Details

Complete active space second-order multiconfigurational perturbation theory (CASPT2) considering the effect of the dynamic electron correlation with MOLCAS 8.4 program package[4] was performed on the basis of single-crystal X-ray determined geometries of **1** and **2** (see Fig. S8 for the calculated model structures of **1** and **2**).

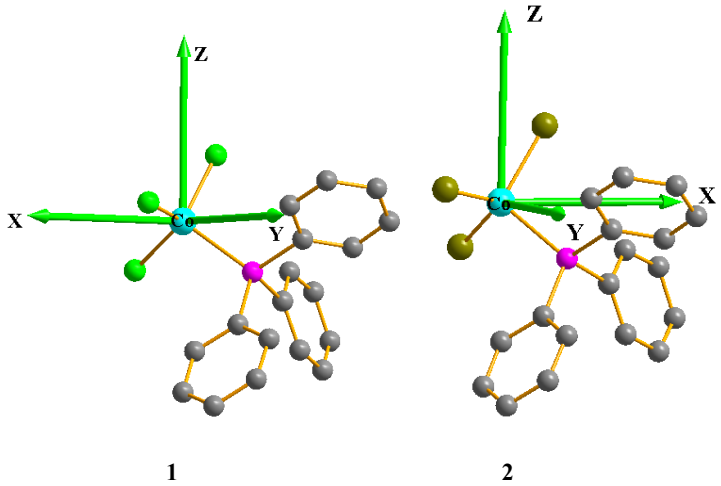

Fig. S10 Calculated model structures of individual Co^{II} fragments. H atoms are omitted for clarity.

For the first complete-active-space self-consistent field (CASSCF) calculation, the basis sets for all atoms are atomic natural orbitals from the MOLCAS ANO-RCC library: ANO-RCC-VTZP for magnetic center ion Co^{II}; VTZ for close Br, Cl and P atoms; VDZ for distant atoms. The calculations employed the second order Douglas-Kroll-Hess Hamiltonian, where scalar relativistic contractions were taken into account in the basis set. The active electrons in 5+5′ active orbitals include all d electrons (CAS(7 in 5+5′)) in the CASSCF calculations. To exclude all the doubts, we calculated all the roots in the active orbitals. The effect of the dynamical electronic correlation was applied using CASPT2 based on the first CASSCF calculation. After that, the spin-orbit coupling was handled separately in the restricted active space state interaction (RASSI-SO)

procedure.[5, 6] We have mixed the maximum number of spin-free state which was possible with our hardware (all from 10 quadruplets and 40 doublets). SINGLE_ANISO[7-9] program was used to obtain zero-field splitting parameters D (E) (cm^{-1}), $\boldsymbol{g}$ tensors, energy levels, magnetic axes, *et al.* based on the above CASPT2/RASSI-SO calculations.

To deeply analyze the magnetic anisotropy, ORCA 4.2 calculations[10] were performed with CASSCF, followed by N-electron valence second-order perturbation theory (NEVPT2). The spin-orbit coupling (SOC) operator used was the efficient implementation of the multicenter spin-orbit mean-field (SOMF) concept developed by Hess et al.[6] The spin-spin contributions (SSC) to the D values were also included although they are very small for our complexes. The NEVPT2[11-14] calculation with seven 3d electrons in five Co 3d-based orbitals (CAS(7, 5)). In the calculations, the orbitals were determined for the average of 10 $S = 3/2$ and 40 $S = 1/2$ roots. All calculations were performed with triple-ζ with one polarization function def2-TZVP[15-17] basis set for all atoms.

Table S6 Calculated spin-free energies (cm^{-1}) of the lowest ten terms (S = 3/2) of **1** and **2** using CASPT2/RASSI-SO with MOLCAS 8.4.

spin-free states	**1**	**2**
	E/cm^{-1}	E/cm^{-1}
1	0.0	0.0
2	2817.1	2684.3
3	3209.6	3174.9
4	3616.5	3290.2
5	4091.9	3654.0
6	8444.8	7742.8
7	8446.9	7747.4
8	16389.8	16959.3
9	16403.9	16994.2
10	19328.5	18823.7

Table S7 Calculated weights of the five most important spin-orbit-free states for the lowest two spin-orbit states of **1** and **2** using CASPT2/RASSI-SO with MOLCAS 8.4.

	Spin-orbit states	Energy (cm^{-1})	Spin-free states, Spin, Weights				
1	1	0.0	1,1.5,0.9580	3,1.5,0.0171	4,1.5,0.0106	2,1.5,0.0102	5,1.5,0.0019
	2	78.2	1,1.5,0.9728	3,1.5,0.0091	2,1.5,0.0084	4,1.5,0.0073	5,1.5,0.0013
2	1	0.0	1,1.5,0.9580	3,1.5,0.0178	4,1.5,0.0166	2,1.5,0.0038	5,1.5,0.0019
	2	63.6	1,1.5,0.9690	2,1.5,0.0101	4,1.5,0.0096	3,1.5,0.0089	5,1.5,0.0012

Table S8 Contributions of the excited states (with relative energy cm^{-1}) to *D* and *E* values (cm^{-1}) for **1** and **2** using NEVPT2 with ORCA 4.2.

Fragments	State No.	Mult	Energy, cm^{-1}	Contribution, cm^{-1}	Contribution, cm^{-1}
				D	*E*
1	1	4	2923.4	–10.039	0.000
	2	4	2972.8	16.636	15.973
	3	4	2974.4	16.618	–15.973
2	1	4	2384.2	–12.687	0.000
	2	4	2705.1	16.733	16.629
	3	4	2707.0	16.718	–16.629

Table S9 Relative energies (cm^{-1}) of ligand field one-electron states (in the basis of d-AOs) of **1** and **2** from AILFT analysis using NEVPT2 with ORCA 4.2.

Fragments	No.	LF one-electron state	Energy, cm^{-1}
1	1	$0.97\ d_{yz} - 0.15\ d_{xy} - 0.15\ d_{x2-y2}$	0.0
	2	$0.97\ d_{xz} - 0.16\ d_{xy} + 0.15\ d_{x2-y2}$	2.1
	3	$0.94\ d_{xy} + 0.27\ d_{x2-y2}$	3761.4
	4	$-0.94\ d_{x2-y2} + 0.27\ d_{xy}$	3763.9
	5	$1.00\ d_{z2}$	3933.5
2	1	$-0.97\ d_{yz} - 0.24\ d_{x2-y2}$	0.0
	2	$0.97\ d_{xz} + 0.24\ d_{xy}$	1.9
	3	$0.95\ d_{xy} - 0.23\ d_{xz}$	3094.6
	4	$0.95\ d_{x2-y2} - 0.23\ d_{yz}$	3096.5
	5	$1.00\ d_{z2}$	3929.6

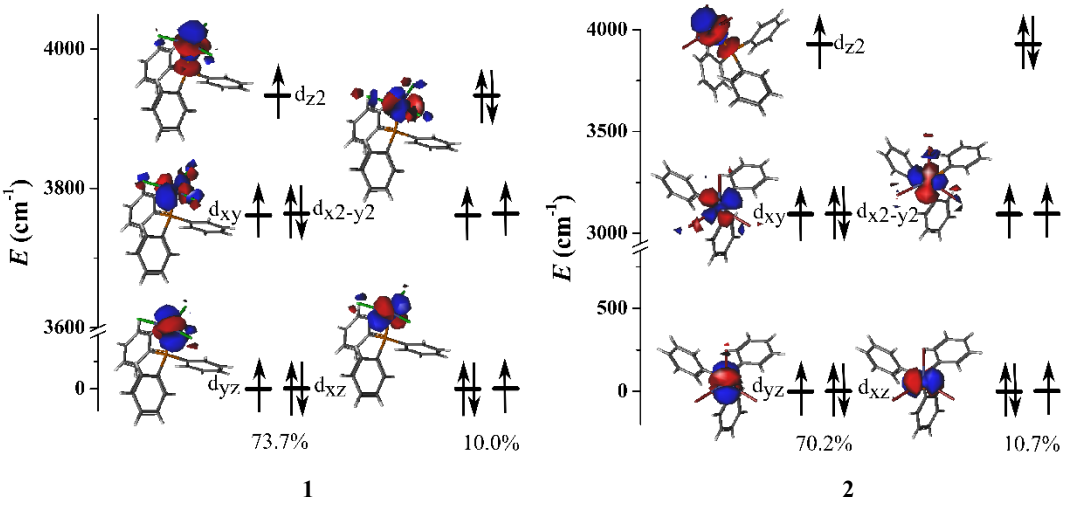

Fig. S11 Orbital energies computed for the ground states of **1** and **2** using NEVPT2 with ORCA 4.2. The percentage mention reveals the percent of the corresponding configuration mixing.

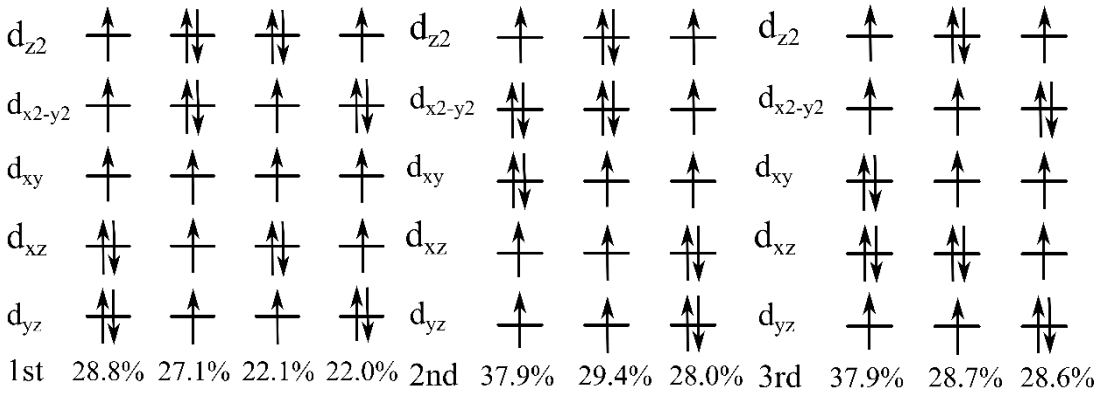

1

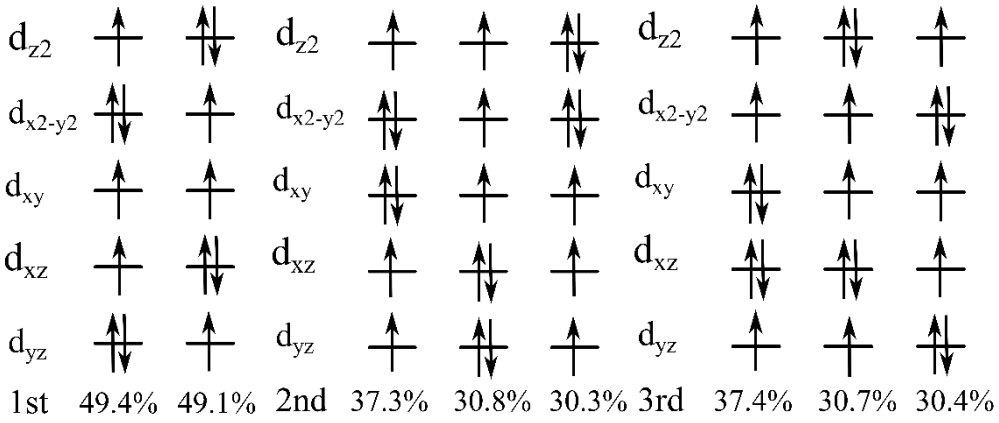

2

Fig. S12 Multi-determinant wavefunction of the selected excited states having important contributions to *D* tensor for **1** and **2**. The computed CI coefficients that are larger than 10% are shown above.

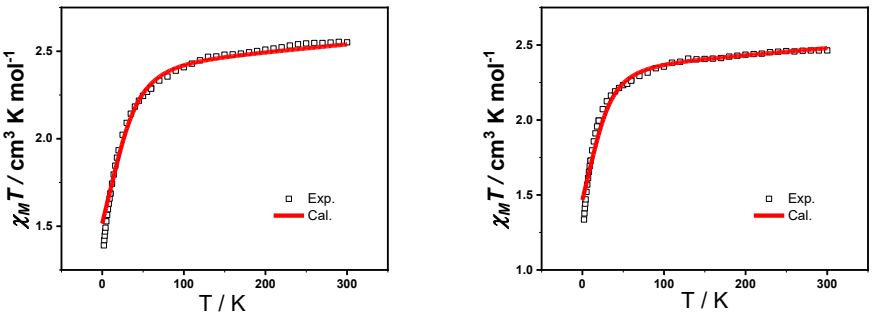

Fig. S13 Comparisons of the calculated (solid line) and the experimental magnetic susceptibilities for **1**–**2**.

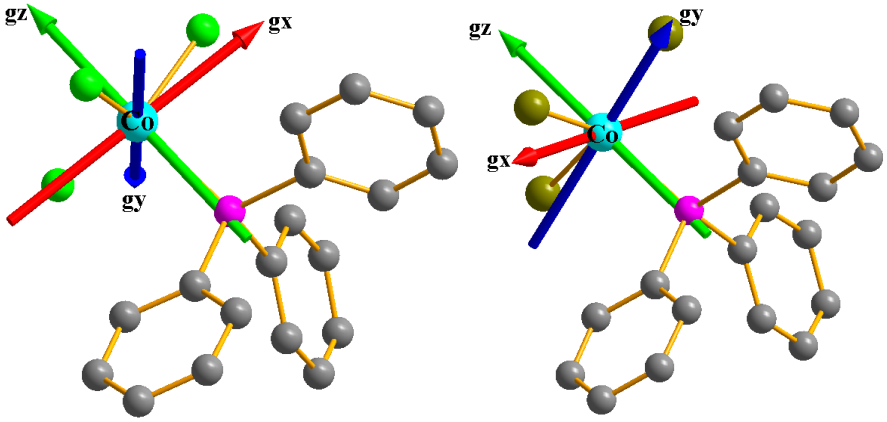

Fig. S14 Orientations of the local magnetic axes (red: g_x; blue: g_y; green: g_z) on Co^{II} ions of **1** and **2** in their ground spin-orbit states using CASPT2/RASSI-SO with MOLCAS 8.4.

Notes and references

1. M. Llunell, D. Casanova, J. Cirera, P. Alemany and S. Alvarez, *Shape Program Vision 2.1,* 2013.
2. S. Alvarez, P. Alemany, D. Casanova, J. Cirera, M. Llunell and D. Avnir, *Coord. Chem. Rev.*, 2005, **249**, 1693-1708.
3. N. F. Chilton, R, P. Anderson, L. D. Turner, A. Soncini and K. S. Murray, *J. Comput. Chem.*, 2013, **34**, 1164-75.
4. F. Aquilante, J. Autschbach, R. K. Carlson, L. F. Chibotaru, M. G. Delcey, L. De Vico, I. Fdez Galván, N. Ferré, L. M. Frutos, L. Gagliardi, M. Garavelli, A. Giussani, C. E. Hoyer, G. Li Manni, H. Lischka, D. Ma, P. Malmqvist, T. Müller, A. Nenov, M. Olivucci, T. B. Pedersen, D. Peng, F. Plasser, B. Pritchard, M. Reiher, I. Rivalta, I. Schapiro, J. Segarra-Martí, M. Stenrup, D. G. Truhlar, L. Ungur, A. Valentini, S. Vancoillie, V. Veryazov, V. P. Vysotskiy, O. Weingart, F. Zapata and R. Lindh, *J. Comput. Chem.*, 2016, **37**, 506-541.
5. P. Å. Malmqvist, B. O. Roos and B. Schimmelpfennig, *Chem. Phys. Letters*, 2002, **357**, 230–240.
6. B. A. Heß, C. M. Marian, U. Wahlgren and O. Gropen, *Chem. Phys. Letters*, 1996, **251**, 365-371.
7. L. F. Chibotaru, L. Ungur and A. Soncini, *Angew. Chem. Int. Ed.*, 2008, **47**, 4126-4129.
8. L. Ungur, W. Van den Heuvel and L. F. Chibotaru, *New J. Chem.*, 2009, **33**, 1224-1230.
9. L. F. Chibotaru, L. Ungur, C. Aronica, H. Elmoll, G. Pilet and D. Luneau, *J. Am. Chem. Soc.*, 2008, **130**, 12445-12455.
10. F. Neese, *Max-Plank institute for bioinorganic chemistr,* Mülheim an der Ruhr, Germany, 2019.
11. C. Angeli, R. Cimiraglia and J. P. Malrieu, *J. Chem. Phys.*, 2002, **117**, 9138-9153.
12. C. Angeli, R. Cimiraglia and J.-P. Malrieu, *Chem. Phys. Letters*, 2001, **350**, 297-305.
13. C. Angeli and R. Cimiraglia, *Theor. Chem. Acc.*, 2002, **107**, 313-317.
14. C. Angeli, R. Cimiraglia, S. Evangelisti, T. Leininger and J. P. Malrieu, *J. Chem. Phys.*, 2001, **114**, 10252-10264.

15. A. Schäfer, C. Huber and R. Ahlrichs, *J. Chem. Phys.*, 1994, **100**, 5829-5835.

16. A. Schäfer, H. Horn and R. Ahlrichs, *J. Chem. Phys*, 1992, **97**, 2571-2577.

17. F. Weigend and R. Ahlrichs, *Phys. Chem. Chem. Phys.*, 2005, **7**, 3297-3305.

18. O. Y. Vassilyeva, E. A. Buvaylo, V. N. Kokozay, B. W. Skelton, C. Rajnak, J. Titis and R. Boca, *Dalton Trans*, 2019, **48**, 11278-11284.

19. J. M. Zadrozny, J. Liu, N. A. Piro, C. J. Chang, S. Hill and J. R. Long, *Chem. Commun.*, 2012, **48**, 3927-3929.

20. K. A. Schulte, K. R. Vignesh and K. R. Dunbar, *Chem. Sci.*, 2018, **9**, 9018-9026.

21. S. Gomez-Coca, E. Cremades, N. Aliaga-Alcalde and E. Ruiz, *J. Am. Chem. Soc.*, 2013, **135**, 7010-7018.

22. D. Pinkowicz, F. J. Birk, M. Magott, K. Schulte and K. R. Dunbar, *Chem. Eur, J.*, 2017, **23**, 3548-3552.

23. F. Yang, Q. Zhou, Y. Zhang, G. Zeng, G. Li, Z. Shi, B. Wang and S. Feng, *Chem Commun*, 2013, **49**, 5289-91.

24. R. Boča, J. Miklovič and J. Titiš, *Inorg. Chem.*, 2014, **53**, 2367-2369.

25. M. R. Saber and K. R. Dunbar, *Chem Commun*, 2014, **50**, 12266-9.

26. C. Rajnák, A. Packová, J. Titiš, J. Miklovič, J. Moncol' and R. Boča, *Polyhedron*, 2016, **110**, 85-92.

27. Y.-Q. Zhai, Y.-F. Deng and Y.-Z. Zheng, *Dalton Trans.*, 2018, **47**, 8874-8878.

28. A. K. Mondal, M. Sundararajan and S. Konar, *Dalton Trans*, 2018, **47**, 3745-3754.

29. J. Hruby, D. Dvorak, L. Squillantini, M. Mannini, J. van Slageren, R. Herchel, I. Nemec and P. Neugebauer, *Dalton Trans.*, 2020, **49**, 11697-11707.